Highly catalytically active CeO2-x based heterojunction nanostructures with mixed micro/meso-porous architectures

Sajjad S. Mofarah,* Luisa Schreck, Claudio Cazorla, Xiaoran Zheng, Esmaeil Adabifiroozjaei, Constantine Tsounis, Jason Scott, Reza Shahmiri, Yin Yao, Roozbeh Abbasi, Kourosh Kalantar-Zadeh, Yuan Wang, Hamidreza Arandiyan, Leigh Sheppard, Esmail Doustkhah, Pramod Koshy, and Charles C. Sorrell*

ABSTRACT: Achieving high densities of accessible active sites in catalysts, which depend principally on the architecture of nanostructures, is critical to obtain enhanced performance. The present work introduces a template-free, high-yield, and flexible approach to fabricate 3D, mesoporous, CeO_{2-x} nanostructures in centimeter-scale that are comprised of extremely thin holey 2D nanosheets. The method involves conversion of a stacked, 2D, Ce-based coordination polymer by controlling the removal kinetics of organic species. The resultant polycrystalline 2D-3D CeO_{2-x} exhibits a large density of defects as well as outstanding surface areas of 251 m^2 g^{-1}. This mesoporous nanomaterial yields superior CO conversion performance ($T_{90\%}$ = 148˚C). Further improvements in catalysis were attained by synthesis CeO_{2-x} -based transition metal oxides (TMOs) hetero-nanostructures, for which structural analyses and first principles simulations revealed active sites associated with the TMOs. This versatile fabrication technique delivers new pathways to engineer nanostructures and advance their functionalities for catalysis.

KEYWORDS: *Holey Two-Dimensional, Defect-rich CeO_2, Porous Heterojunction Nanostructure, Ce-based Coordination Polymers*

■ INTRODUCTION

Three dimensional (3D) mesoporous metal oxides (MOs) hold great promise in catalysis through increasing accessibility of the active sites relative to bulk materials. Nonetheless, the use of sacrificial templates, which generally is employed to introduce the pores and allow the formation of the 3D structures, makes the fabrication process complex and of low efficiency. Certain shortcomings also apply to various etching techniques for creating pores in 3D scaffolds[1,2]. In porous structures, the walls of the 3D scaffolds limit the number of active sites to only the surface and subsurface of these 3D units. The recently developed techniques involving the creation of nanoholes in two dimensional (2D) MOs has facilitated the accessibility of active sites by exposing greater surface area,[3-5] thus making these materials attractive for surface-sensitive applications in energy, sensing, and heterogeneous catalysis.[6-8] Further, the intrinsic polycrystallinity of these holey 2D structures can overcome the critical shortcoming of irreversible restacking of pristine 2D nanosheets.[9, 10] Recent advances in the synthesis of polycrystalline holey 2D MOs include the heterogeneous deposition of mixed transition metal oxides (TMOs) on graphene nanosheets as a sacrificial template[11] and the synthesis of holey TMOs by etching pristine 2D TMOs.[12-14] Despite considerable improvements in the performances of these nanostructures, challenges, such as complex synthesis procedures, use of

surfactants and templates, excessive nanosheet thicknesses,[15] and low yields, limit their practical applicabilities. Unlike TMOs, there are few reports of pristine 2D rare earth oxides (REOs), none of which exhibit intrinsically layered structures. Consequently, complex methods of self-assembly have been applied as an alternative to exfoliation, which typically is applied to convert layered materials to 2D nanostructures.[16, 17] Although such nanostructures have shown outstanding catalytic and photocatalytic performance,[18] they have the disadvantage of low-yield production.[19]

The present work reports a new synthesis route to fabricate multidimensional 2D-3D structures consisting of 2D holey nanosheets of CeO_{2-x} (or TMO-decorated CeO_{2-x}) that stack to form mesoporous 3D nanostructures with enhanced catalytic functionalities.

RESULTS

Fabrication of Porous CeO_2 Hexagonal tubes Derived from Cerium-Based Coordination Polymer (Ce-CP)

In order to synthesize the 2D-3D CeO_{2-x}, a novel Ce-CP, which is the sole precursor, was fabricated electrochemically at room temperature.[9] This resulted in the formation of free-standing hexagonal tubes grown vertically on fluorine-doped tin oxide (FTO) substrates. The Ce-CP has the molecular formula of $Ce(TCA)_2(OH)_2{\cdot}2H_2O$ (TCA – trichloroacetate) and the β-axis view of the structure is shown schematically in Figure 1a, where the unit cell with triclinic structure (space group $P\bar{1}$) is also defined. The Ce ions are covalently bonded to the O^{2-} ions of H_2O, OH^-, and TCA, thereby forming stacked layers of thickness 1.04 nm (α-spacing). However, the terminating Cl^- ions of TCA at the opposite interfaces are electrostatically attracted to protons, as evidenced from zeta potential (ξ) measurements (Figure S1). It is significant that the Ce-CP can be transformed into CeO_2, shown in Figure 1b, through simple oxidation. This transformation is shown schematically in Figure 1c, where a dense distribution of nanopores results from TCA removal and formation of a porous CeO_2 nanotube (Ce-NT); the obtained Ce-NT is shown by scanning electron microscopy (SEM) imaging (Figure 1d-f).

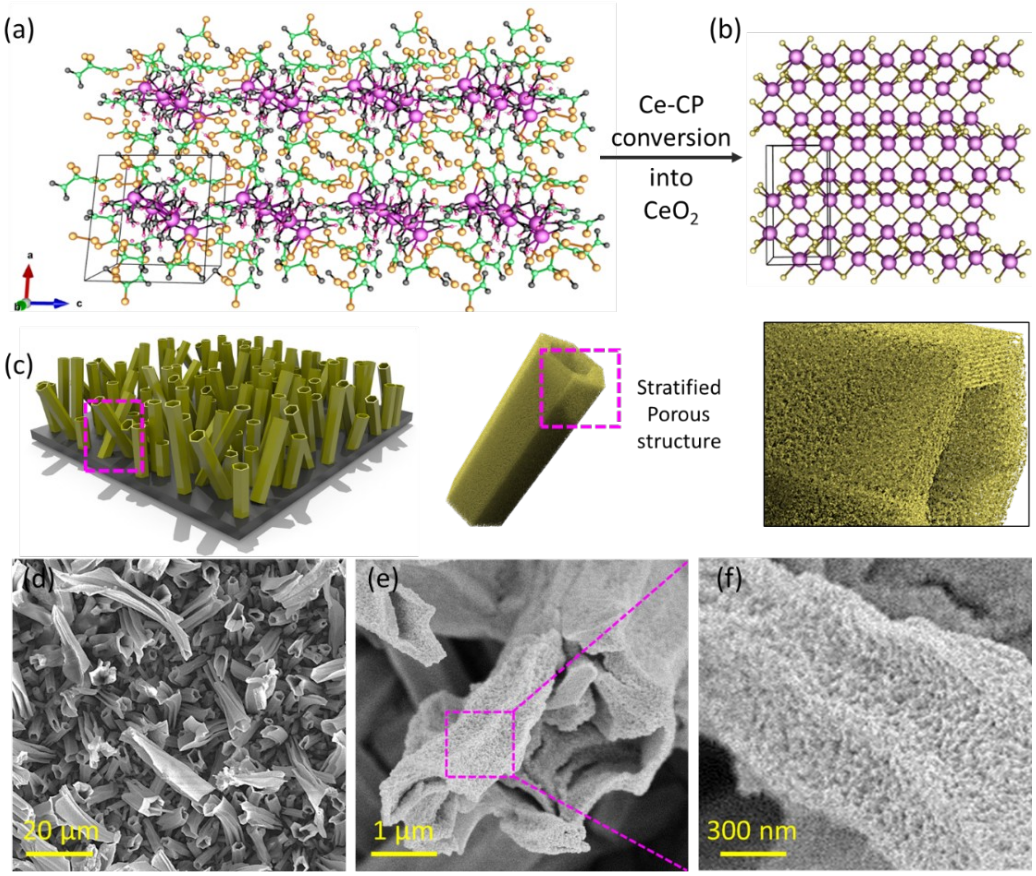

Figure 1. (a) Schematic of β-axis projection of Ce-CP molecule; (b) schematic of CeO_2 molecule; (c) schematic and (d-f) SEM images of porous CeO_2 nanotubes on FTO substrates.

Fabrication of 2D-3D CeO_{2-x} Scaffold Through Exfoliation of Ce-CP. The simple exfoliation and rapid oxidation of the Ce-CP provide the means of tailoring the resultant CeO_2 architectures. The formation of 2D-3D oxides involves a two-step process of exfoliation of the bulk-layered Ce-CP in polar triethanolamine (TEA), followed by heat treatment the suspension at ~450°C (heating rate 3°C/min) in air, as shown in Figure 2a. The exfoliation results in a stable colloidal system (ξ = +34 V) of individual Ce-CP monolayers (Figure S1). The heating process leads to conversion of the Ce-CP layers into CeO_{2-x} through evaporation of the interlayer-trapped TEA, resulting in a mesoporous 3D structure. The importance of the kinetics in the engineering of the final nanostructures (Figure S2) is shown by the effects of the heating rate. Figure 2b, c shows that a slow heating rate (0.2°C/min) allowed the laminar evaporation of TEA, resulting in a stacked solid macrolayer of CeO_{2-x} covered by intact hemispheres (Figure S2a). An intermediate heating rate (1.0°C/min) caused fracture of the hemispheres owing to gas exudation; however, the hemispherical shapes were retained (Figure S2b, c). In contrast, fast heating rates (3.0°C/min) caused energetic volumetric evaporation of TEA, nanostructural disruption, and formation of thick mesoporous macrolayers (Figure 2d, e). The significance of TEA in exfoliation is highlighted by contrasting with the conventional oxidation of metal-based coordination polymers (MCPs), where the original microstructure is retained[20-22]. Higher magnifications (Figure 2f-h) reveal nanostructures consisting of clustered 2D nanosheets in 3D scaffold morphology. High-angle annular dark field (HAADF)

imaging and the selected area diffraction (SAED) pattern (Figure 2i) illustrates the polycrystallinity nature of the nanosheets, consisting of CeO_2 crystallite sizes of 2-4 nm and high concentrations of pores sizes of 3-5 nm. Energy dispersive X-ray (EDX) elemental mapping of the holey nanosheet (Figure 2j) illustrates homogenous distributions of cerium and oxygen. Atomic force microscopy (AFM) imaging (Figure 2k) shows an example of a nanosheet with a thickness of ~4 nm, which represents ~8 unit cells of cubic CeO_2, although the average thickness of the sheets was ~15 nm, which still represents remarkably thin holey nanosheets.

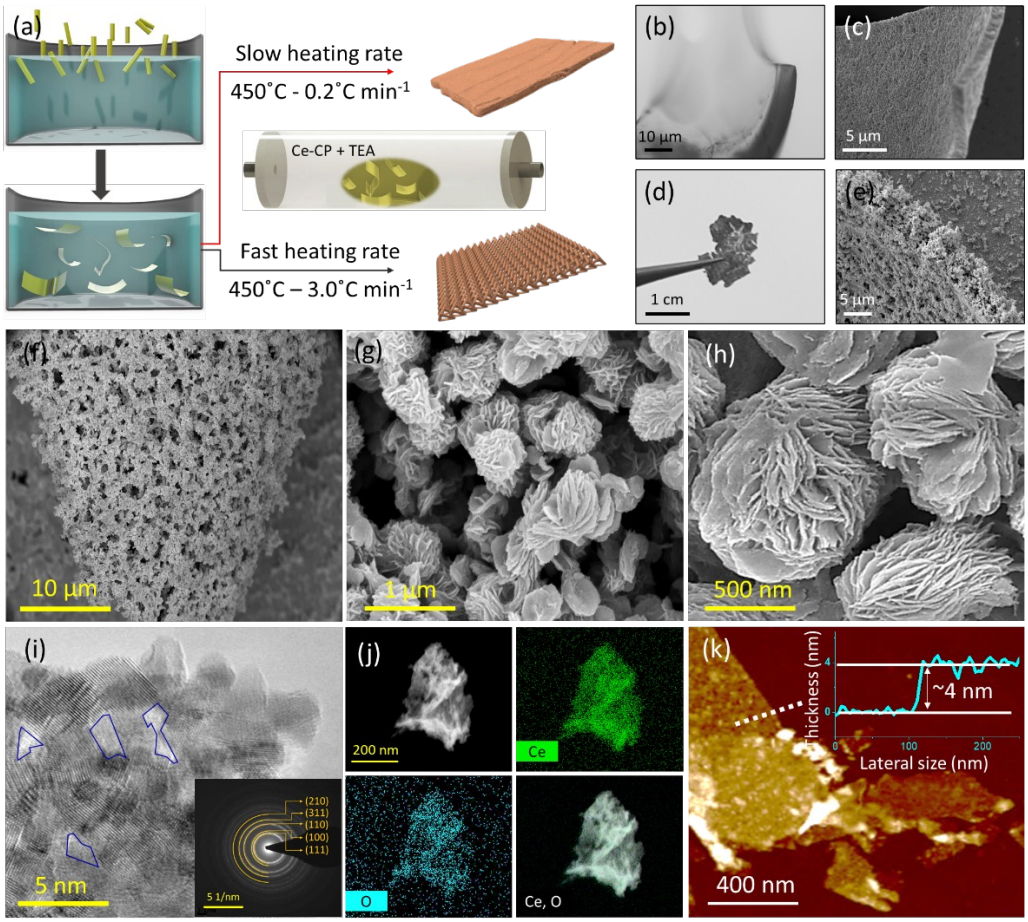

Figure 2. (a) Schematic of two-step process of Ce-CP nanotube exfoliation in stirred TEA solution and oxidation at 450°C in air into stacked CeO_{2-x} macrolayers. (b-e) CeO_{2-x} morphologies derived from Ce-CP. (f-h) SEM images of 2D-3D CeO_{2-x}. (i) HAADF image and SAED of holey 2D CeO_{2-x} nanosheet (holes outlined). (j) EDX elemental mapping of holey 2D CeO_{2-x} nanosheet. (k) AFM image (step height in white dotted line) and corresponding height profile of holey 2D CeO_{2-x} nanosheet.

The wide-ranging applicability of the fabrication process is demonstrated by the one-step synthesis of various heterogeneous nanostructures through the addition of water-soluble transition metal salts ($CuNO_3$ or $Mn(NO_3)_2$) during the Ce-CP exfoliation step. Subsequent transformation resulted in the formation of 2D-3D CeO_{2-x} decorated homogeneously with CuO (Ce-Cu) or MnO (Ce-Mn) of unchanged morphologies, in common with the pristine 2D-3D CeO_{2-x}. Characterization data for the nanostructural features of the Ce-Cu and Ce-Mn are given in Figures S4-S7.

Defect Analysis of 2D-3D CeO_{2-x} and Heterojunction Nanostructures. Figure 3 illustrates the results for structural, defect, and surface analyses of the nanostructures. As shown in Figure 3a, the Ce^{3+} concentration ($[Ce^{3+}]$) of the mesoporous 2D-3D CeO_{2-x} was determined by X-ray photoelectron spectroscopy (XPS) to be 27 at% ($[V_O^{\bullet\bullet}]$ = 13.5 at%) using the standard correlation for $[Ce^{3+}]$.[23] This level can be compared with the data for the electron energy loss spectroscopy (EELS) data shown in Figure 3b. Applying the linear relationship between the M_5/M_4 peak intensity ratio and the $[V_O^{\bullet\bullet}]$,[24, 25] a value of 12.8 at% was obtained for the latter, which is in relatively good agreement with that calculated from $[Ce^{3+}]$. The laser Raman microspectroscopy spectra in Figure 3c reveal the F_2g vibrational mode of Ce-O at ~464 cm^{-1}, confirming the presence of CeO_2.[26] The spectra for Cu-Ce and Mn-Ce reveal asymmetrical peak broadening of the F_2g peak at ~464 cm^{-1} owing to quantum confinement effects.[26, 27] There also are two additional peaks at ~580 cm^{-1} and ~1147 cm^{-1} for all three materials, which are attributed to the defect-induced mode (D) and 2nd order longitudinal optical mode (2LO), respectively, associated with $V_O^{\bullet\bullet}$.[26, 28, 29] The XPS data for the TMO-decorated CeO_{2-x} in Figure 3d,e reveal shoulder peaks (green), which are indicative of Mn^{2+} and Cu^{2+} satellites, supporting the presence of MnO (Figures S4 and S5) and CuO (Figures S6 and S7),[30, 31] as confirmed by the associated SEM and EDX data. The Brunauer-Emmett-Teller (BET) specific surface areas (SSA) were determined to be 51, 251, 230, and 160 $m^2 \cdot g^{-1}$ for the Ce-NT, CeO_{2-x}, Mn-Ce, and Cu-Ce nanostructures, respectively, as shown in Figure 3f. The sizes and volumes of the pores are also tabulated (Table S1). The significant effect of exfoliation on the increase in the SSA and the pore volume is shown by the respective fourfold and eightfold increases for the Ce-NT and the 2D-3D CeO_{2-x}. The higher SSA for Mn-Ce relative to that of Cu-Ce is attributed to the formation of a compact laminated nanostructure (Figure S6) for the latter compared to the clustered 2D nanosheets in 3D spherical morphology for the former (Figure S4).

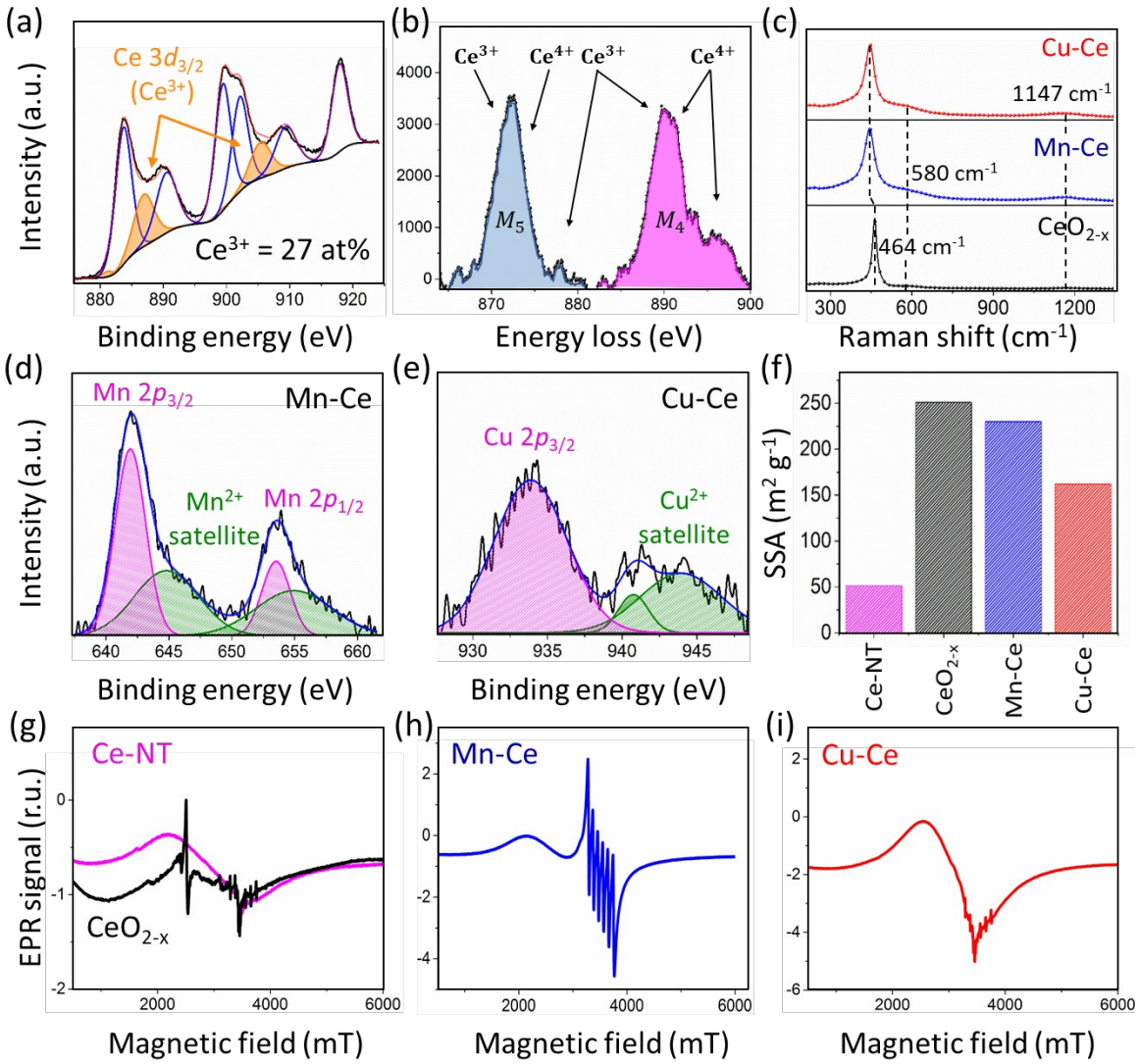

Figure 3. Characterization of nanostructures: (a) XPS Ce 3d spectrum of 2D-3D CeO_{2-x}. (b) EELS spectrum of 2D-3D CeO_{2-x}. (c) Laser Raman microspectra 2D-3D CeO_{2-x}, Mn-Ce, Cu-Ce. (d) XPS Mn 2p spectrum of Mn-Ce. (d) XPS Cu 2p spectrum of Cu-Ce. (f) SSAs of Ce-NT, 2D-3D CeO_{2-x}, Mn-Ce, Cu-Ce. (g-i) EPR spectra of Ce-NT, 2D-3D CeO_{2-x}, Mn-Ce, Cu-Ce.

Structural defects were probed by electron paramagnetic resonance (EPR) analyses, as shown in Figure 3g-i. For the Ce-NT in Figure 3g, the single hyperfine in Figure S8 indicates only the $Ce^{3+}-O-Ce^{4+}$ defect[32] at a negligible concentration. For the 2D-3D CeO_{2-x} in Figure 3g, the hyperfines in Figure S9 reveal the presence of Ce^{3+}, O_2^-, and $Ce^{3+}-O^-Ce^{4+}$ defects at higher concentrations. These relative concentrations were derived from the total peak areas (using the baselines) of the second integrals of the EPR signal. For the Mn-Ce and Cu-Ce in Figure 3(h,i), the respective hyperfines in Figures S10 and S11 reveal that fabrication of the heterojunction nanostructures introduces new defects associated with TMOs at even higher concentrations than were detected for 2D-3D CeO_{2-x}.

The hyperfine interaction between electrons and nuclei provides information concerning the number and identity of ions and their distances from unpaired electrons. Mn and Cu, with electron configurations of $3d^2$ and $3d^3$, exhibit four

and six absorption signals, respectively, as shown in Figures S10 and S11. Regarding Ce (with electron configurations of $4f^1$ and $5p^6$), Ce^{4+} has no unpaired electrons (EPR-inactive), while Ce^{3+} has a single unpaired electron (EPR-active). However, other EPR peaks can be generated by other unpaired electrons resulting from $V_O^{\bullet\bullet}$, $V_O^{\bullet}$,V_O^{x}, O_2^-, and $Ce^{3+}-O^{-}-Ce^{4+}$ [29]. Table S2 provides the *g*-factors corresponding to the observed hyperfines. The 2D-3D CeO_{2-x}, Cu-Ce, and Mn-Ce exhibit six hyperfine that correspond to values characteristic of the defect $Ce^{3+}-O^-$ [32], albeit with g-factors shifted to lower values relative to that of 2.00 for the free electron of Ce-NT. For the Ce-Mn and Ce-Cu, shifted g-factors are effectively the maximal that can be attributed to the Mn ($3d^2$) and Cu ($3d^3$) species, the EPR signals of which are manifested in the form of shoulders on the sharp peaks and rounded humps with the hyperfines. Figures S8-S11 assess the first and second integrals of the hyperfines for all of the nanostructures, revealing the defect and charge carrier concentrations, which are assumed to be electrons as CeO_{2-x} is an *n*-type semiconductor, although it may exhibit *p*-type semiconductivity under some peculiar conditions, owing to the known presence of cerium vacancies ($V_{Ce}^{''''}$).[9]

Further, The decrease in the first integral is owing to the effect of the energy levels of the trapped electrons, while such decrease in the second integral reflects the balance of the annihilation and creation of defects resulting from the introduction of the TMOs. Figure 3c shows that the $[V_O^{\bullet\bullet}]$ for the TMO-decorated heterostructures were greater than that for the 2D-3D mesoporous CeO_{2-x}, which suggests that other defects were annihilated. These were likely surface structural defects that were blocked by the apposition of the TMO particles. This result is supported by the decrease in surface areas of the decorated heterostructures, as shown in Figure 3f. Another source of defects is intervalence charge transfer (IVCT), which can both create and eliminate defect states.[33]

CO-Conversion Catalysis and DFT Simulation. Figure 4a provides the catalytic performance by the nanostructures in terms of the temperatures for 10, 50, and 90% CO conversion ($T_{10\%}$, $T_{50\%}$, $T_{90\%}$). The $T_{10\%}$ value for the Ce-NT sample was 160°C and the $T_{90\%}$ was 372°C, which are consistent with previous reports for pristine micron-sized CeO_2.[34, 35] In contrast, the 2D-3D CeO_{2-x} exhibited an outstanding performance, with a $T_{90\%}$ of 148°C, which is the lowest temperature among the best-performing pristine CeO_{2-x} nanostructures, as shown by the red line in Figure 4b. The data for Mn-Ce and Cu-Ce in Figure 4a show that these heterostructures exhibit $T_{90\%}$ values of 124°C and 88°C, respectively delivering even better catalytic performance relative to the 2D-3D CeO_{2-x} nanostructure. The blue line in Figure 4b shows that Cu-Ce in this work offers a lower $T_{90\%}$ values than that demonstrated by a selection of the best metal- or oxide-CeO_{2-x} heterostructures available. Comparative lists of the best CeO_2 and CeO_2-based nanostructures, their characteristics, and cited references are given in Tables S3 and S4, respectively.

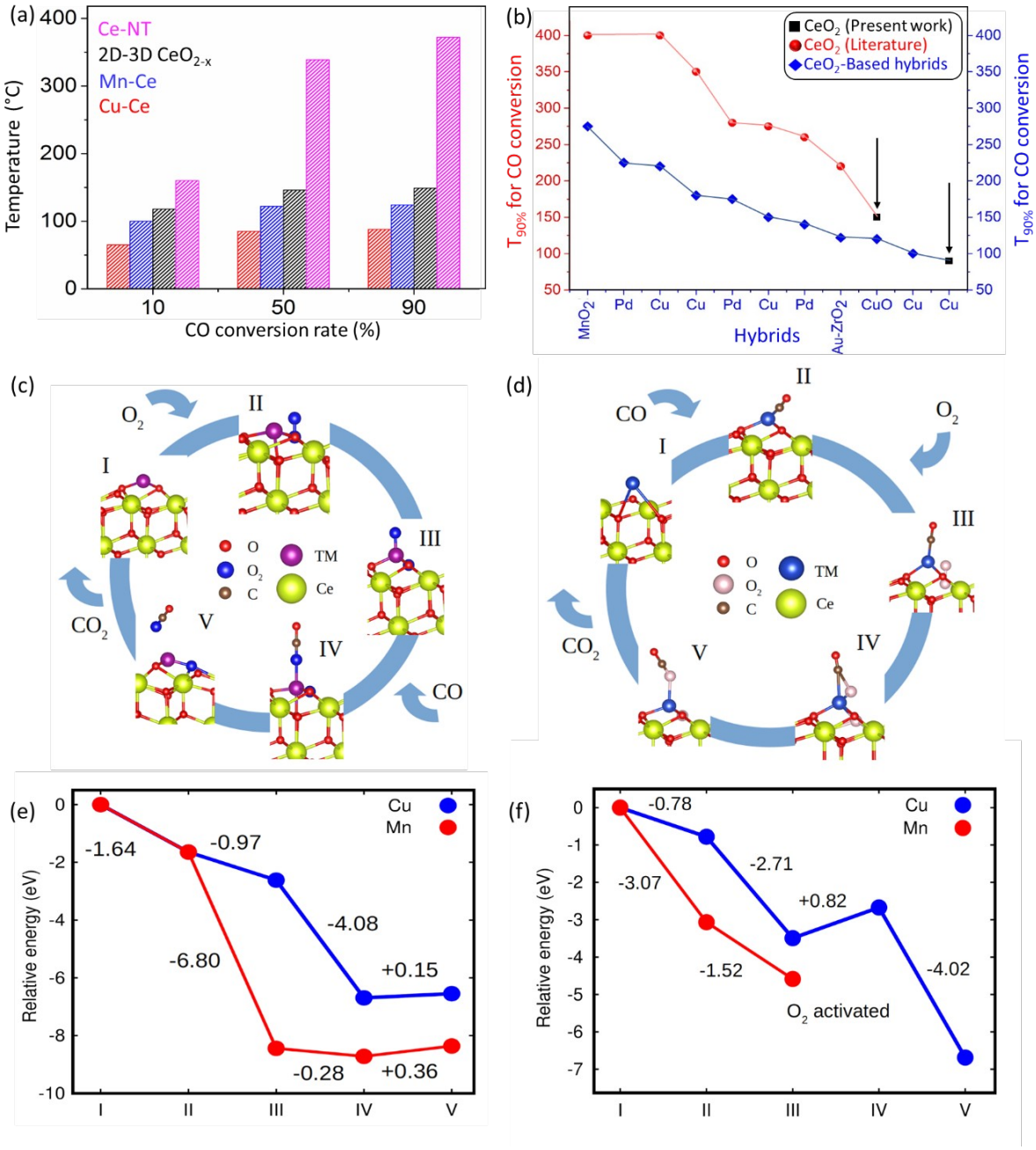

Figure 4. (a) CO oxidation plots for Ce-NT, CeO_{2-x}, Mn-Ce, Cu-Ce. (b) Comparative CO oxidation data for CeO_{2-x} and TMO-decorated CeO_{2-x}. (c) Mechanism 1: CO-oxidation reaction path with initial O_2 adsorption. (d) Mechanism 2: CO-oxidation reaction path with initial CO adsorption. (e) Energy profiles calculated for Mechanism 1. (f) Energy profiles calculated for Mechanism 2.

Although the Cu-Ce nanostructure has a lower specific surface area (SSA) relative to those of the 2D-3D CeO_{2-x} and Mn-Ce nanostructures (Table S1), the former exhibits the highest CO conversion rate at the lowest temperature. This apparent contradiction has been examined by first-principles density functional theory (DFT) calculations of CO and O_2 molecule adsorption on MnO- and CuO-decorated CeO_{2-x}. The calculations reveal that the energetically most favorable sites for O_2 and CO adsorption are in the $V_O^{\cdot\cdot}$ sites on the CeO_{2-x} surface and on

the TM ions, respectively. Consequently, depending on the order of adsorption of the molecules, there are two different possible CO oxidation mechanisms: initial O_2 adsorption in the $V_O^{\bullet\bullet}$ (Figure 4c) or initial CO adsorption on the TM ions on the CeO_{2-x} surface (Figure 4d).

Mechanism 1: Initially (Step I), an O_2 molecule from the atmosphere is immobilized in an oxygen vacancy adjacent to a TM ion on the CeO_{2-x} surface (Step II). Since spontaneous dissociation of the O_2 molecule (which would preclude quenching by O_2 adsorption) and subsequent adsorption of one of the oxygen ions on the TM ion is energetically most favorable, this exothermic process (Figure 4e) takes place (Step III). Owing to the strong attraction between this adsorbed oxygen ion and a CO molecule, the introduction of CO gas results in its adsorption on this oxygen ion (Step IV). This adsorption is favored with a Cu ion relative to an Mn ion (Figure 4e). Finally, the comparative desorption energies of the CO_2 molecule from the Mn ion (0.36 eV) and from the Cu ion (0.15 eV) demonstrates that desorption from the Mn ion is less favored than from the Cu ion. As these are endothermic processes, they require energy inputs, hence the required $T_{90\%}$ values of 124°C and 88°C, respectively.

Mechanism 2: Initially (Step I), a CO molecule is immobilized a TM ion on the CeO_{2-x} surface (Step II). Subsequently, an O_2 molecule from the atmosphere is immobilized in an oxygen vacancy adjacent to a TM ion (Step III). In this case, the dissociation of the O_2 molecule and subsequent adsorption of one of the oxygen ions to form a CO_2 molecule on a TM ion is energetically unfavorable (Figure 4f). In the case of the Cu ion, oxygen ion adsorption is endothermic (0.82 eV) and so occurs upon heating (Step IV). In contrast, with the Mn ion, the more significant difference in Mn-C electronegativity than for Cu-C suggests stronger attraction between the former pair of ions, which suppresses the potential for oxygen ion adsorption to the carbon ion to form the CO_2 molecule. Consequently, with sufficient heating, the O_2 molecule dissociates but adsorption does not occur. In the case of the Cu ion, once the CO_2 molecule is formed, CO_2 desorption (Step V) occurs readily owing to its highly exothermic nature (Figure 4f).

The comparative analysis of the DFT results indicates that Mechanism 1 is likely to be the dominant process in the CO oxidation. Consequently, the low $T_{90\%}$ value for Cu-Ce relative to those reported elsewhere (Table S4) reflects the energetically favorable reaction sequence of three exothermic adsorption reactions followed by a very low endothermic desorption reaction, even though Cu-Ce has the lower SSA of the two heterostructures (Table S1).

■ SUMMARY

The present work introduces a simplified and template-free technique to fabricate multidimensional mesoporous nanostructures. The approach utilizes a Ce-based coordination polymer precursor of stratified structure that can be exfoliated rapidly. During subsequent heating, the stacked-layer precursor converts into macro-mesoporous 2D-3D CeO_{2-x}, depending on control of the kinetics of the transformation. The resultant nanostructures show ultra-high surface areas, defect densities, and pore volumes, which are responsible for unparalleled catalytic performance for CO conversion. The performance was improved further by modifying the 2D-3D CeO_{2-x} via TMO decoration to form heterojunction nanostructures. The enhanced catalytic activities upon using the

TMO modifier, were investigated systematically using structural analyses and first principles DFT simulations. This technique offers new directions for cost-effective and highly controllable fabrication of advanced multidimensional nanocatalysts.

■ ASSOCIATED CONTENT

Supporting information

The Supporting Information is available free of charge on the ACS publications website.

Included are experimental section, figures describing zeta potential, SEM and EDX images of the heterojunction nanostructures, XRD of 2D-3D CeO_{2-x}, Ce-NT, Mn-Ce, and Cu-Ce, data related to EPR analysis and peak assignments for 2D-3D CeO_{2-x}, Ce-NT, Mn-Ce, and Cu-Ce; a table providing CO-conversion results obtained here and compared with other selected best-reported catalysts.

■ AUTHOR INFORMATION

Corresponding Authors

Sajjad S. Mofarah -- *School of Materials Science and Engineering, UNSW Sydney, Sydney, NSW 2052, Australia*;Orcid.org/0000-0002-4835-767X; Email: s.seifimofarah@unsw.edu.au

Charles C. Sorrell -- *School of Materials Science and Engineering, UNSW Sydney, Sydney, NSW 2052, Australia*; Orcid.org/0000-0002-5727-8332;Email: c.sorrell@unsw.edu.au

Authors

Luisa Schreck -- *School of Materials Science and Engineering, UNSW Sydney, Sydney, NSW 2052, Australia*

Claudio Cazorla -- *School of Materials Science and Engineering, UNSW Sydney, Sydney, NSW 2052, Australia*

Xiaoran Zheng -- *School of Materials Science and Engineering, UNSW Sydney, Sydney, NSW 2052, Australia*

Esmaeil Adabifiroozjaei -- *Research Center for Functional Materials (RCFM), National Institute for Materials Science (NIMS), Tsukuba, Ibaraki 305-0047, Japan*

Constantine Tsounis -- *Particles and Catalysis Research Group, School of Chemical Engineering, UNSW Sydney, Sydney, NSW 2052, Australia.*

Jason Scott -- *Particles and Catalysis Research Group, School of Chemical Engineering, UNSW Sydney, Sydney, NSW 2052, Australia.*

Reza Shahmiri -- *School of Materials Science and Engineering, UNSW Sydney, Sydney, NSW 2052, Australia*

Yin Yao -- *Electron Microscopy Unit (EMU), Mark Wainwright Analytical Centre, UNSW Sydney, Sydney, NSW 2052, Australia*

Roozbeh Abbasi -- *School of Chemical Engineering, UNSW Sydney, NSW 2052, Australia*

Kourosh Kalantar-Zadeh -- *School of Chemical Engineering, UNSW Sydney, NSW 2052, Australia*

Yuan Wang -- *School of Chemistry, Faculty of Science, The University of New South Wales, Sydney, NSW 2052, Australia*

Hamidreza Arandiyan -- *Laboratory of Advanced Catalysis for Sustainability, School of Chemistry, University of Sydney, NSW 2006, Australia*

Leigh Sheppard -- *School of Engineering, Western Sydney University, Penrith, NSW, 2751, Australia; orcid.org/0000-0003-3549-6969*

Esmail Doustkhah -- *International Center for Materials Nanoarchitechtonics (MANA), National Institute for Materials Science (NIMS), 1-1 Namiki, Tsukuba, Ibaraki 305-0044, Japan*

Pramod Koshy -- *School of Materials Science and Engineering, UNSW Sydney, Sydney, NSW 2052, Australia*

Author Contributions

S.S.M designed the project, conducted most of the experiments, characterization, provided the first draft, and worked on all the corresponding revisions. L.S. synthesized heterojunction Mn-Ce and Cu-Ce nanostructures and assisted with SEM imaging. C.C. implemented the first-principles simulations, wrote the related section, and commented on the final version of the draft. E.A. performed EELS characterization and commented on the final version of the draft. C.T. and J.S. conducted the CO-conversion tests and provided catalytic results. R.S. conducted the EPR tests and provided the corresponding analysis. Y.Y. conducted AFM imaging. R.A. assisted with experimental design and revision of the drafts. K.K.Z. commented on all the drafts and revised the final versions. Y.W. and H.A. assisted with analyzing the catalytic performance, commented, and worked on the final versions of the draft. L.S. assisted in setting up the electrochemical cell, conducting Ce-CP synthesis, and revision of the drafts. E.D. performed SSA test for Ce-NT and commented on the final version of the draft. P.K. contributed to the data analyses and revised final version of the manuscript. C.C.S. worked on all drafts of the manuscript and supervised the overall project.

Funding

This work has been supported by the Australian Research Council (DP170104130). The authors are grateful for access to the characterization facilities provided by the Mark Wainwright Analytical Centre, UNSW Sydney and beam time at the Wombat beamline of the Australian Nuclear Science and Technology Organization (ANSTO). S.S.M. is pleased to acknowledge UIPA and RTP scholarship support from UNSW Sydney. E.A. Acknowledges the financial support (JSPS KAKENHI Grant Number: 18F18064) provided by the Japan Society for the Promotion of Science.

Notes

The authors declare no competing financial interest.

■ ACKNOWLEDGMENTS

We acknowledge the Mark Wainwright Analytical Centre, Sydney, Australia for provision of characterization facilities and assisting with data analysis. Further, we acknowledge Setareh M. Pour for providing the schematic images in this work.

■ REFERENCES

(1) Zhang, Q.; Lee I.; Ge J.; Zaera F.; Yin Y. Surface-Protected Etching of Mesoporous Oxide Shells for the Stablization of Metal Nanocatalysts. *Adv. Func. Mater.* **2010**, 20 (14), 2201-2214.

(2) Doustkhah E.; Ide Y.; Bursting Exfoliation of a Microporous Layered Silicate to Three-Dimenssionally Meso-Microporous Nanosheets for Improved Molecular Recognition. *ACS Appl. Nano. Mater.* **2019**, 2 (12), 7513-7520.

(3) Shen, K.; Zhang, L.; Chen, X.; Liu, L.; Zhang, D.; Han, Y.; Chen, J.; Long, J.; Luque, R.; Li, Y.; Chen, B. Ordered Macro-Microporous Metal-Organic Framework Single Crystals. *Science* **2018**, 359 (6372), 206-210.

(4) Lan, K.; Liu, Y.; Zhang, W.; Liu, Y.; Elzatahry, A.; Wang, R.; Xia, Y.; Al-Dhayan, D.; Zheng, N.; Zhao, D. Uniform Ordered Two-Dimensional Mesoporous TiO_2 Nanosheets from Hydrothermal-Induced Solvent-Confined Monomicelle Assembly. *J. Am. Chem. Soc.* **2018**, 140 (11), 4135-4143.

(5) Peng, L.; Fang, Z.; Li, J.; Wang, L.; Bruck, A. M.; Zhu, Y.; Zhang, Y.; Takeuchi, K. J.; Marschilok, A. C.; Stach, E. A.; Takeuchi, E. S.; Yu, G. Two-Dimensional Holey Nanoarchitectures Created by Confined Self-Assembly of Nanoparticles via Block Copolymers: From Synthesis to Energy Storage Property. *ACS nano* **2018**, *12* (1), 820-828.

(6) Xiong, J.; Di, J.; Xia, J. X.; Zhu, W. S.; Li, H. M. Surface Defect Engineering in 2D Nanomaterials for Photocatalysis. *Adv. Funct. Mater.* **2018**, 28, 39.

(7) Voiry, D.; Shin, H. S.; Loh, K. P.; Chhowalla, M. Low-Dimensional Catalysts for Hydrogen Evolution and CO_2 Reduction. *Nat. Rev. Chem.* **2018**, 2, 0105.

(8) Voiry, D.; Shin, H. S.; Loh, K. P.; Chhowalla, M. Low-Dimensional Catalysts for Hydrogen Evolution and CO_2 Reduction. *Nat. Rev. Chem.* **2018**, 2, 0105.

(9) Mofarah, S. S.; Adabifiroozjaei, E.; Pardehkhorram, R.; Assadi, M. H. N.; Hinterstein, M.; Yao, Y.; Liu, X.; Ghasemian, M. B.; Kalantar-Zadeh, K.; Mehmood, R.; Cazorla, C.; Shahmiri, R.; Bahmanrokh, G.; Bhattacharyya, S.; Spadaro, M. C.; Arbiol, J.; Lim, S.; Xu, Y.; Arandiyan, H.; Scott, J.; Koshy, P.; Sorrell, C. C. Coordination Polymer to Atomically Thin, Holey, Metal-Oxide Nanosheets for Tuning Band Alignment. *Adv. Mater.* **2019**, 31 (52), 1905288.

(10) Peng, L.; Fang, Z.; Zhu, Y.; Yan, C.; Yu, G. Holey 2D Nanomaterials for Electrochemical Energy Storage. *Nat. Energy* **2018**, 8 (9), 1702179.

(11) Peng, L.; Xiong, P.; Ma, L.; Yuan, Y.; Zhu, Y.; Chen, D.; Luo, X.; Lu, J.; Amine, K.; Yu, G. Holey Two-Dimensional Transition Metal Oxide Nanosheets For Efficient Energy Storage. *Nat. Commun.* **2017,** 8, 15139.

(12) Wen, W.; Wu, J. M.; Cao, M. H. Facile Synthesis of a Mesoporous Co_3O_4 Network for Li-Storage via Thermal Decomposition of an Amorphous Metal Complex. *Nanoscale* **2014**, 6, (21), 12476-12481.

(13) Zhang, G.; Ren, L.; Yan, Z.; Kang, L.; Lei, Z.; Xu, H.; Shi, F.; Liu, Z. H. Rational Design and Controllable Preparation of Holey MnO_2 Nanosheets. *Chem. Commun.* **2017**, 53 (20), 2950-2953.

(14) Bo, X.; Li, Y.; Hocking, R. K.; Zhao, C. NiFeCr Hydroxide Holey Nanosheet as Advanced Electrocatalyst for Water Oxidation. *ACS Appl. Mater. Inter.* **2017**, 9 (47), 41239-41245.

(15) Fang, Z.; Peng, L.; Qian, Y.; Zhang, X.; Xie, Y.; Cha, J. J.; Yu, G. Dual Tuning of Ni-Co-A (A = P, Se, O) Nanosheets by Anion Substitution and Holey Engineering for Efficient Hydrogen Evolution. *J. Am. Chem. Soc.* **2018**, 140 (15), 5241-5247.

(16) Sun, Y.; Liu, Q.; Gao, S.; Cheng, H.; Lei, F.; Sun, Z.; Jiang, Y.; Su, H.; Wei, S.; Xie, Y. Pits Confined in Ultrathin Cerium(IV) Oxide for Studying Catalytic Centers in Carbon Monoxide Oxidation. *Nat. Commun.* **2013**, 4, 2899.

(17) Yu, T.; Lim, B.; Xia, Y. Aqueous-Phase Synthesis of Single-Crystal Ceria Nanosheets. *Angew. Chem. Int. Ed.* **2010**, 49 (26), 4484-4487.

(18) S. Mofarah, S.; Adabifiroozjaei, E.; Wang, Y.; Arandiyan, H.; Pardehkhorram, R.; Yao, Y.; Assadi, M. H. N.; Mehmood, R.; Chen, W.-F.; Tsounis, C.; Scott, J.; Lim, S.; Webster, R.; Zhong, V.; Xu, Y.; Koshy, P.; Sorrell, C. C. Assembly of Cerium-Based Coordination Polymer into Variant Polycrystalline 2D–3D CeO_{2-x} Nanostructures. *J. Mater. Chem. A* **2020**, 8, 4753-4763.

(19) Zhu, Z.; Yin, H.; He, C.T.; Al-Mamun, M.; Liu, P.; Jiang, L.; Zhao, Y.; Wang, Y.; Yang, H.G.; Tang, Z.; Wang, D.; Chen, X. M.; Zhao H. Ultrathin Transition Metal Dichalcogenide/3d Metal Hydroxide Hybridized Nanosheets to Enhance Hydrogen Evolution Activity. *Adv. Mater.* **2018**, 30(28), 1801171.

(20) Zou, F.; Hu, X.; Li, Z.; Qie, L.; Hu, C.; Zeng, R.; Jiang, Y.; Huang, Y. MOF-Derived Porous ZnO/$ZnFe_2O_4$/C Octahedra with Hollow Interiors for High-Rate Lithium-Ion Batteries. *Adv. Mater.* **2014**, 26 (38), 6622-8.

(21) Salunkhe, R. R.; Tang, J.; Kamachi, Y.; Nakato, T.; Kim, J. H.; Yamauchi, Y. Asymmetric Supercapacitors Using 3D Nanoporous Carbon and Cobalt Oxide Electrodes Synthesized from a Single Metal–Organic Framework. *ACS Nano* **2015**, 9 (6), 6288-6296.

(22) Zhang, F.; Chen, C.; Xiao, W.-m.; Xu, L.; Zhang, N. CuO/CeO_2 Catalysts with Well-Dispersed Active Sites Prepared from $Cu_3(BTC)_2$ Metal–Organic Framework Precursor for Preferential CO Oxidation. *Catal. Commun.* **2012**, 26, 25-29.

(23) Mehmood, R.; Wang, X.; Koshy, P.; Yang, J. L.; Sorrell, C. C. Engineering Oxygen Vacancies through Construction of Morphology Maps for Bio-Responsive Nanoceria for Osteosarcoma Therapy. *CrystEngComm* **2018**, 20 (11), 1536-1545.

(24) Feng, B.; Sugiyama, I.; Hojo, H.; Ohta, H.; Shibata, N.; Ikuhara, Y. Atomic Structures and Oxygen Dynamics of CeO_2 Grain Boundaries. *Sci. Rep.* **2016**, 6, 20288.

(25) Mofarah, S. S.; Adabifiroozjaei, E.; Yao, Y.; Koshy, P.; Lim, S.; Webster, R.; Liu, X.; Khayyam Nekouei, R.; Cazorla, C.; Liu, Z.; Wang, Y.; Lambropoulos, N.; Sorrell, C. C. Proton-Assisted Creation of Controllable Volumetric Oxygen Vacancies in Ultrathin CeO_{2-x} for Pseudocapacitive Energy Storage Applications. *Nat. Commun.* **2019**, 10, 2594.

(26) Wu, Z.; Li, M.; Howe, J.; Meyer, H. M.; Overbury, S. H. Probing Defect Sites on CeO_2 Nanocrystals with Well-Defined Surface Planes by Raman Spectroscopy and O_2 Adsorption. *Langmuir* **2010**, 26 (21), 16595-16606.

(27) Kosacki, I.; Suzuki, T.; Anderson, H. U.; Colomban, P. Raman Scattering and Lattice Defects in Nanocrystalline CeO_2 Thin Films. *Solid State Ion.* **2002**, 149, 99-105.

(28) Spanier, J. E.; Robinson, R. D.; Zhang, F.; Chan, S.-W.; Herman, I. P. Size-Dependent Properties ofCeO_{2-y} Nanoparticles as Studied by Raman Scattering. *Phys. Rev. B* **2001**, 64 (24), 2454071-8.

(29) López, J. M.; Gilbank, A. L.; García, T.; Solsona, B.; Agouram, S.; Torrente-Murciano, L. The Prevalence of Surface Oxygen Vacancies Over the Mobility of Bulk Oxygen in Nanostructured Ceria for the Total Toluene Oxidation. *Appl. Catal. B: Environ.* **2015**, 174-175, 403-412.

(30) Ilton, E. S.; Post, J. E.; Heaney, P. J.; Ling, F. T.; Kerisit, S. N. XPS Determination of Mn Oxidation States in Mn (hydr)oxides. *Appl. Surf. Sci.* **2016**, 366, 475-485.

(31) Zhang, Q.; Huang, L.; Kang, S.; Yin, C.; Ma, Z.; Cui, L.; Wang, Y. CuO/Cu_2O Nanowire Arrays Grafted by Reduced Graphene Oxide: Synthesis, Characterization, and Application in Photocatalytic Reduction of CO_2. *RSC Adv.* **2017**, 7 (69), 43642-43647.

(32) Wang, L.; Yu, Y.; He, H.; Zhang, Y.; Qin, X.; Wang, B. Oxygen Vacancy Clusters Essential for the Catalytic Activity of CeO_2 Nanocubes for o-xylene Oxidation. *Sci Rep.* **2017**, 7, 12845.

(33) Chen, W. F.; Mofarah, S. S.; Hanaor, D. A. H.; Koshy, P.; Chen, H. K.; Jiang, Y.; Sorrell, C. C. Enhancement of Ce/Cr Codopant Solubility and Chemical Homogeneity in TiO_2 Nanoparticles through Sol-Gel versus Pechini Syntheses. *Inorg. Chem.* **2018**, 57 (12), 7279-7289.
(34) Zhou, X.; Ling, J.; Sun, W.; Shen, Z. Fabrication of Homogeneously Cu^{2+}/La^{3+}-Doped CeO_2 Nanosheets and their Application in CO Oxidation. *J. Mater. Chem. A* **2017**, 5 (20), 9717-9722.
(35) Kim, K.; Yoo, J. D.; Lee, S.; Bae, M.; Bae, J.; Jung, W.; Han, J. W. Simple Descriptor to Rapidly Screen CO Oxidation Activity on Rare-Earth Metal-Doped CeO_2: From Experiment to First-Principles. *ACS Appl. Mater. Inter.* **2017**, 9 (18), 15449-15458.

Graphic Abstract

The present work reports a new template-free, high-yield, and flexible approach to fabricate centimeter-scale, 3D, mesoporous, CeO_{2-x} based nanostructures that are comprised of holey 2D nanosheets as thin as ~4 nm. The method involves conversion of a newly developed, bulk-layered, Ce-based coordination polymer by controlled kinetics of removal of organic species. Further, the flexibility of the synthesis approach allows fabrication of various TMO-based heterojunction nanostructures with outstanding surface areas and densities of active sites, which yield superior CO conversion performance.